

Design improvement of circular molten carbonate fuel cell stack through CFD Analysis

Original

Design improvement of circular molten carbonate fuel cell stack through CFD Analysis / Verda, Vittorio; Sciacovelli, Adriano. - In: APPLIED THERMAL ENGINEERING. - ISSN 1359-4311. - (2011), pp. 2740-2748.
[10.1016/j.applthermaleng.2011.04.046]

Availability:

This version is available at: 11583/2488180 since:

Publisher:

Elsevier

Published

DOI:10.1016/j.applthermaleng.2011.04.046

Terms of use:

This article is made available under terms and conditions as specified in the corresponding bibliographic description in the repository

Publisher copyright

(Article begins on next page)

DESIGN IMPROVEMENT OF CIRCULAR MOLTEN CARBONATE FUEL CELL STACK THROUGH CFD ANALYSIS

Vittorio Verda

Department of Energetics
Politecnico di Torino, Italy
vittorio.verda@polito.it

Adriano Sciacovelli

Department of Energetics
Politecnico di Torino, Italy
adriano.sciacovelli@polito.it

ABSTRACT

Molten carbonate fuel cell (MCFC) is a promising technology for distributed power generation. The core of a MCFC power generation unit is the stack, where various fuel cells are connected together in series and parallel in order to obtain the desired voltage and power. Stack geometry and configuration are major engineering topics, as inhomogeneous temperature or mass fractions cause inefficient performances of the fuel cells, as efficiency and power smaller than the expected and shorter lifetime. A detailed model is a useful tool to improve stack performances, through design improvements.

In this paper, a 3D model of a stack composed of 15 circular MCFC, considering heat, mass and current transfer as well as chemical and electrochemical reactions is presented. The model validation is conducted using some preliminary experimental data obtained for a MCFC stack developed in the Fabbricazioni Nucleari laboratories. These results are examined in order to improve the stack configuration. It is shown that power density may be increased of about 20% through double side feeding. In addition, the average temperature gradients in the axial direction are reduced of more than 70%. Significant reductions in the temperature gradients, especially in transversal direction, can be achieved by adjusting the mass flow rate of cathodic gas supplied to the various cells.

Keywords: Molten Carbonate Fuel Cells, CFD model, Stack model, Design improvement.

NOMENCLATURE

$D_{i,eff}$	Effective diffusion coefficient ($m^2 s^{-1}$)
D_{ij}	Mass diffusion coefficient ($m^2 s^{-1}$)
E_k	Apparent activation energy (K^{-1})
F	Faraday constant ($96487 C mol^{-1}$)
h	Specific enthalpy ($J kg^{-1}$)
\vec{i}	Current density vector ($A m^{-2}$)
\vec{j}_i	Diffusive flux of species i ($kg m^{-2} s^{-1}$)
j_0	Exchange current density ($A m^{-2}$)
K	Permeability (m^2)
k	Thermal conductivity ($W m^{-1} K^{-1}$)
k_{eff}	Effective thermal conductivity ($W m^{-1} K^{-1}$)
M	Molecular weight ($kg mol^{-1}$)
n_e	Number of electrons
p	Pressure (Pa)
R	Universal gas constant ($W mol^{-1} K^{-1}$)
s	Specific entropy ($J kg^{-1} K^{-1}$)
S_i	Species source term ($kg m^{-3} s^{-1}$)
S_h	Heat source term ($W m^{-3} s^{-1}$)
T	Temperature (K)
v	Specific volume ($m^3 kg^{-1}$)
V	Velocity ($m s^{-1}$)
\vec{V}	Velocity vector ($m s^{-1}$)

Greek symbols

ϕ Potential (V)

β	Transfer coefficient
ε	Porosity
η_{act}	Activation overpotential (V)
μ	Viscosity (m s^{-2})
ρ	Density (kg m^{-3})
σ	Electric conductivity ($\Omega^{-1} \text{m}^{-1}$)
τ	Tortuosity
ω_i	Mass fraction of species i

INTRODUCTION

Molten Carbonate Fuel Cell (MCFC) is a fuel cell which electrolyte is a ceramic matrix filled of sodium and potassium carbonates, in molten form. The operating temperature is usually between 600°C and 700°C in order to allow effective ion conduction and prevent from rapid voltage degradation. Carbonate ions are produced on the cathodic side, by the electrochemical reaction



and migrate through the electrolyte to the anodic side, where the following reaction occurs



One of the main advantages of MCFCs is the potential high efficiency that can be achieved with hybrid cycles, where the fuel cell is integrated with a microturbine. This kind of plants is still not commercial, but several installations are now operating. Some of the issues are related with plant lifetime and discrepancies between theoretical and real performances. Detailed models of MCFC can be used to understand the phenomenological behavior [1], evaluate the effects of possible changes in the design [2], examine the operating conditions for diagnosis [3] or control purposes [4], predict the performances of a cell within a complex plant, such as a hybrid plant [5]. Various single cell and stack models have been proposed in the last 30 years. A comprehensive review of the models proposed in the eighties and nineties is available in [6]. Because of the computational limitations, associated to both hardware and software, significant hypotheses had to be formulated which nowadays may be overcome. An hypothesis which is still popular, especially in the case of transient simulation [7], is that of plug flow. This allows one to reduce the number of computational cells, as discussed in [8]. The full 3D analysis is usually adopted for planar structures [9], sometimes using a coarse mesh.

Other possible approaches in the case of stack modeling are based on repeated cells with proper boundary conditions to account for the position within the stack [11], on model reduction (2D) [10] and on quasi-3D models obtained through 1D [3], 2D [12] or network models [13] with proper inputs from parallel layers.

This paper aims to investigate possible improvements that can be achieved by introducing design changes at stack level. A prototype composed by 15 circular molten carbonate fuel cells, manufactured by the Italian company Fabbricazioni Nucleari [14], is considered. The analysis is conducted through a full 3D model of the stack. The model accounts for heat, mass and charge transfer; chemical and electrochemical reactions are considered through proper boundary conditions and source terms in the partial differential equations. The results show that non-homogeneous distributions of temperature and reactant mass fractions occur both at cell level and stack level. This means that there are significant differences in temperatures and concentrations between zones in a cell and also between the various cells. This behavior, already shown in previous studies conducted on different cell and stack geometries [4, 12, 15, 16] and confirmed by the experimental analysis, is responsible for undesired behaviors: efficiencies or power densities lower than expected, due to larger resistances, and reduced lifetime, due to high temperatures and large temperature gradients. Possible design changes that allows one to reduce gradients at cell level have been examined in [17]. Here possible design changes at stack level are proposed. These changes are basically conducted by intervening on the oxidant mass flow rate supplied to the various cells. The stack configuration analyzed in this paper allows one to increase the mass flow rate to the cells at higher temperature, obtaining a more homogeneous distribution. This subject is not widely treated in the literature. In [18] a mixed experimental-numerical approach is used to improve the performance of a MCFC stack. A simple numerical model is used to adjust some orifices and homogenize the flow distribution. No thermal analysis is conducted. In [19] two stack configurations, co-flow and counter-flow, are compared using experimental analysis. In [20] the reverse problem is considered, i.e. the effects of flow maldistribution are simulated for a SOFC stack.

MCFC STACK GEOMETRY AND MODEL

The stack is composed of an external supporting structure in stainless steel, where distribution channels are located, and an internal portion, which includes the electrodes, the electrolyte and the porous distribution layers.

Figure 1 shows the mesh of the computational domain, which corresponds to a quarter of the entire stack. This shows the 15 cells,

together with the axial inlet and outlet ducts for fuel and cathodic gas. Fuel flows from the bottom to the top and air from the top to the bottom. These gases enter each single cell through radial ducts also represented in the figure. In total there are 4 inlet anodic channels, 4 inlet cathodic channels, 4 outlet anodic channels and 4 outlet cathodic channels.

Figure 2 shows a schematic of a single fuel cell, together with the external structure, the 16 axial ducts (A-D are the inlet anodic ducts, E-H the inlet cathodic ducts, I-L the outlet anodic ducts and M-P the outlet cathodic ducts) and the radial ducts. To show the various layers of the cells and the main flow paths, two cross sections are drawn in Figure 3.

The fuel cell consists of a total of 11 layers: 2 external supporting layers in stainless steel, 2 porous inlet channels (for fuel and cathodic gas), 2 stainless steel plate with small axial orifices in the center, 2 outlet channels, anode, electrolyte and cathode. In the inlet channels, the fluid enters from the four radial channels: those connected with ducts A-D distribute the fuel to the inlet anodic channel (in Figure 3, the axial duct A and the corresponding radial duct is represented), and those connected with ducts E-H distribute the cathodic gas to the inlet cathodic channel. These gases flow from the periphery towards the center and then through the axial orifices, reaching the porous outlet channels. In these channels, the fluids permeate the electrodes while flowing towards the periphery, where the exhausts exit through the radial ducts (those connected with axial ducts I-H and M-P. In Figure 3, the axial duct K and the corresponding radial duct are represented).

This structure has the advantage to be easy to build. Both the external and the internal structures are constituted of a superimposition of layers. This allows one to obtain the axial and radial channels through laser cutting. In addition, this arrangement is modular, thus a different size is obtained by stacking a different number of layers (including both the internal and external structure), without issues concerning fluid distribution. A stack of 15 cells is then obtained by simple superposition of 15 groups of layers as these shown in Figure 3. Stack dimensions are presented in Table 1.

The cell matrix is made of γ -LiAlO₂. This is obtained in the FN laboratories through a productive process from the moulding plastic technology, which is fast and does not require any solvents. The electrolyte is the eutectic Li-K carbonate melt.

A model used for stack design purpose should solve mass (i.e. fluid flow and conservation of species), heat and current transfer. Fluid flow consists of the continuity equation (3) together with the momentum equation (4):

$$\rho \nabla \cdot \vec{V} = 0 \quad (3)$$

$$\rho \cdot \vec{V} \cdot \nabla \vec{V} = -\nabla p + \mu \cdot \nabla^2 \vec{V} - \frac{\mu}{K} \vec{V} \quad (4)$$

where ρ is the fluid density, \vec{V} is the velocity vector, p is the pressure, μ the viscosity, K the permeability. The last term in equation (4) only appears in the porous media (Brinkman equation), while it is zero in the channels (Navier-Stokes equation).

Mass flow rates \dot{m} , mass fractions ω_i and temperatures are specified on the inlet cross-sections. On the outlet cross-sections, pressure is set as equal to the ambient pressure, namely:

$$p = p_0 \quad (5)$$

Since the MCFC stack geometry presents an angular periodicity of 90°, periodic boundary conditions are imposed along the two longitudinal planes of the computational domain represented in Figure 1 for equations (1) and (2). These conditions are also imposed for all the other partial differential equations. Finally, velocities are set to zero at the solid walls.

The conservation of gas species is written for H₂, CO, CO₂, H₂O on the anode side and O₂, CO₂, N₂ on the cathode side. For the general species this is written in the form

$$\nabla \cdot \rho \cdot \vec{V} \cdot \omega_i = -\nabla \cdot \vec{J}_i + S_i \quad (6)$$

where ω is the mass fraction, and \vec{J}_i the diffusion flux which is expressed through the Maxwell-Stefan equation

$$\vec{J}_i = \rho D_{i,eff} \nabla \omega_i + \frac{\rho \omega_i}{M} - M \sum_j D_{j,eff} \nabla \omega_j - \nabla M \sum_j D_{j,eff} \omega_j \quad (7)$$

The first term on the right hand side is Fick diffusion due to concentration gradients [21], while the other terms are the correction factors to enforce the Stefan-Maxwell equations for the multi-component diffusion. M is the molar mass and $D_{i,eff}$ coincides with the binary diffusivity in the gas channels [22]. Binary diffusivities are calculated through the Fuller-Schettler-Giddings correlation [24]:

$$D_{ij} = \frac{0.143 \times 10^{-6} \cdot T^{1.75}}{p M_{ij}^{1/2} \left(\frac{1}{v_i^{1/3}} + \frac{1}{v_j^{1/3}} \right)} \quad (8)$$

$$M_{ij} = 2 \left(\frac{1}{M_i} + \frac{1}{M_j} \right)^{-1} \quad (9)$$

Diffusivities (8) are corrected as effective binary diffusivities [23, 24] in order to take the influence of the porous media on the diffusion rate into account

$$D_{ij,eff} = \frac{\varepsilon}{\tau} D_{ij} \quad (10)$$

The source term in equation (6) accounts for the water-gas shift reaction in the anode. Internal steam reforming in the anode has not been considered, as there is no specific active catalyst for this reaction [25]. Generation and destruction of species due to the electrochemical reactions are computed through proper boundary conditions on the surface between the electrolyte and the electrode. This approach is acceptable as the electrochemical reactions occur in a small thickness [26]. These conditions are expressed through Faraday's law:

$$\vec{J}_i \cdot \vec{n} = \frac{\vec{i} \cdot \vec{n}}{n_e F} M_i \quad (11)$$

where \vec{n} is the unit vector perpendicular to the surface, \vec{i} the current, n_e the number of electrons involved in the electrochemical reaction of the i -th species and F the Faraday's constant.

A convective flow condition

$$\vec{J}_i \cdot \vec{n} = 0 \quad (12)$$

is assumed on the outlet sections, while mass fluxes are set to zero at the solid walls. The continuity is imposed at the electrode/outlet channel interfaces.

Heat transfer is solved by means of the energy equation, which has been written in the form:

$$\nabla \cdot \vec{V} \rho h = \nabla \cdot k_{eff} \nabla T + S_h \quad (13)$$

where h is the fluid enthalpy and k_{eff} is the effective conductivity, which is the gas conductivity in the channels and the weighted mean conductivity of gas conductivity and solid matrix conductivity [Anderson et al]:

$$k_{eff} = \varepsilon \cdot k_g + (1 - \varepsilon) \cdot k_s \quad (14)$$

where the subscripts g and s refer to the gas and the solid phase respectively. In equation (9r) ε is the porosity of the porous media. Properties of gaseous species are obtained from [27].

The source term S_h accounts for Joule heating effect due to ohmic resistance, i.e.:

$$S_h = \sigma \nabla^2 \phi \quad (15)$$

where σ is the electrical conductivity and ϕ the potential. Electrolyte conductivity is expressed as the function of local temperature:

$$\sigma = \sigma_0 \exp(-E_k/T) \quad (16)$$

where the parameters σ_0 and E_k are shown in Table 2. Conductivities of the electrodes are assumed as constant.

The reversible heat and the activation losses associated to the electrochemical reactions are accounted through the following boundary condition applied to electrode/electrolyte interface [28]:

$$\vec{\varphi} \cdot \vec{n} = \frac{\vec{i} \cdot \vec{n}}{2F} T \cdot \Delta S + (\vec{i} \cdot \vec{n}) \cdot \eta_{act} \quad (17)$$

Convective flow condition is assumed on the outlet sections:

$$-k \nabla T \cdot \vec{n} = 0 \quad (18)$$

The current transfer is computed through the following conservation equation:

$$\nabla^2 \phi = 0 \quad (19)$$

The cell potential is imposed on the top and bottom surfaces. In addition, a voltage drop due to activation overpotential is set on the surface between the electrodes and electrolyte. These are computed through the Butler-Volmer equation [29, 30]:

$$\vec{i} \cdot \vec{n} = j_0 \cdot \left(e^{\frac{\beta \cdot n_e \cdot F}{R \cdot T} \eta_{act}} - e^{\frac{(1-\beta) \cdot n_e \cdot F}{R \cdot T} \eta_{act}} \right) \quad (20)$$

The exchange current at the cathode side j_0 depends on the partial pressure of the reacting gas:

$$j_{0,cat} = j_{0,cat}^0 (p_{CO_2})^{r_1} (p_{O_2})^{r_2} \quad (21)$$

The values of $j_{0,cat}^0$, r_1 and r_2 are taken from [30]. The anode exchange current density is obtained as follow [30]:

$$j_{0,an} = j_{0,an}^0 (p_{H_2})^{(1-\beta)/2} (p_{CO_2} p_{H_2O})^{\beta/2} \quad (22)$$

The values of the various parameters are shown in Table 2.

Grid sensitivity is performed on the single cell, because of the large computational cost that would require the analysis of the entire stack. Three different grids have been used to check the mesh sensitivity. The number of cells adopted are about 60000, 90000 and 120000, respectively. Temperature profiles along the cell radius are presented in Figure 4. The curves show that 60000 cells are sufficient to avoid significant changes in the results due to the mesh choice.

To check the model, three points at different voltage are calculated for a single cell and compared with the experimental polarization curve. This comparison is shown in Figure 5.

STACK SIMULATION

The stack simulation is performed in order to highlight differences in the performances of the various fuel cells. The characteristics of the fluids entering the stack are presented in Table 3. In the experimental setup, fuel is obtained from a reforming reactor unit located on the top of the stack.

Figure 6 shows the power density distribution in the various cells. The largest value, 612 W/m², occurs in the cell number 10 on the portion close to the external row of the axial orifices. The minimum value, 136 W/m², occurs in the external areas of the first cell. The average power density is 287.1 W/m².

In order to improve the efficiency and lifetime of the fuel cell it is necessary to improve this distribution, making it more homogeneous. To achieve this result it is necessary to modify the design, intervening on the causes of such distribution, i.e. the non homogeneous mass fractions and temperatures, as explained in the following.

Figure 7 shows the hydrogen mass fraction distribution. The largest concentration occurs in the central area of each cell, close to the outer portion where the orifices connecting the inlet anodic channel and the outlet anodic channel are located. This is the area with the maximum amount of fresh fuel reaching the anode. The concentration is smaller in the centre because of the smaller amount of fuel reaching this zone. The concentration decreases towards the four outlet sections because of the fuel consumption due to the electrochemical reaction (see equation 11). In the external areas far from the outlet ducts mass fractions are small because the fluid velocity is very small [33].

Hydrogen concentration is similar in all the cells because the fuel mass flow rate is similar and the hydrogen consumption is the same, as each cell produces the same current.

The oxygen mass fraction in the cathode of four fuel cells is shown in figure 8. The mass fraction is small in the center because of the large current density in this zone. The highest concentration takes place in the outer part of the central area, then it decreases from the center to the periphery, because of the electrochemical reaction. This distribution is similar in the various cells.

Figure 9 shows the axial temperature profile at R= 24 mm, calculated using the 3D model, compared with the experimental values obtained in the testing lab. The lowest temperature occurs in the cell located on the top (cell 1), which is the cell closer to the inlet anodic gas. The highest temperature occurs in the cell number 10.

In the cells, temperature decreases from the center towards the periphery, which is the consequence of heat generation due to electrochemical reactions, activation losses (equation 20) and joule heating (equation 15). Figure 10 shows the temperature distribution in the cell number 10, which is the one with the largest temperature and also the largest temperature gradients. The minimum temperature, 876 K, occurs close to the section where the anodic gas enters the fuel cell. Temperature gradients in the cells can be reduced through changes in the fluid distribution inside the cell, as discussed hereafter.

In order to discuss possible ways to improve the stack, the power density in various point of the stack is expressed as the function of temperature and position. This is presented in Figure 11. The three markers correspond to different radial positions. Points with the same marker correspond to different cells. These points are characterized by similar reactant composition but different temperature, thus different voltage and similar current density. In contrast, the three points of the same cell are characterized by considerably different reactant composition and slightly different temperature.

These results show that there are margins to increase the stack performances through changes in the fluid distribution system, both at cell level and stack level. At cell level, it is possible to obtain a more homogeneous fluid distribution by tracing Y-shaped distribution channels [34] on the stainless steel plates above the porous media [17] and by increasing the number of outlet radial ducts. This allows one to reduce the concentration gradients in each cell, which results in a more homogeneous distribution of the current density. The

present paper is focused on possible improvements that can be achieved at stack level. These improvements can be obtained by acting on the temperature distribution, which involve the fluid distribution management.

STACK IMPROVEMENTS

Possible changes in the fluid distribution design are analyzed in the present section. These changes are summarized in Table 4.

A first way to improve the stack consists in adjusting the mass flow rate on the cathodic side, so that a larger flow reaches the hotter cells. This may be achieved by properly reducing the diameter of the radial ducts for the colder cells. Such modification is expected not to affect the performance of these cells, as the cathodic flow is significantly larger than necessary. The temperature distribution (design 2) compared to that of the initial design (design 1) is presented in Figure 12. The peak temperature at $R=24$ mm drops from 904.5 K to 894 K, which is beneficial from structural viewpoint as the temperature gradients reduce. The temperature profile in the design 2 is always below that for design 1; this is due to the reduced current density, which also means a reduced source term. The effect on the power density is thus negative. This quantity reduces to 271 W/m^2 . Nevertheless, it must be considered that the inlet temperature of fuel can be increased as far as the maximum temperature is below the maximum temperature in design 1. The temperature profile obtained by increasing of 10°C the inlet temperature of the anodic gas (which may be obtained through heat exchange with the exhausts) is also shown in Figure 12 (design 3). This arrangement allows one to obtain a power density closer to that in design 1. The difference between maximum and minimum temperature reduces from about 109 K to about 86 K. The figure also shows that it is possible to further increase the inlet temperature of the anodic gas and thus increase the power density and reduce the temperature gradients. Figure 13 shows that the change in the distribution of cathodic gas produces reductions in the temperature gradients in transversal direction. The difference between maximum and minimum temperature in cell 10 is reduced from 33°C to 21°C . This is a major advantage with respect to design 1.

Further improvement of the stack design consists in supplying both the anodic and cathodic gases from two sides of the stack. This means that the anodic gas enters from sections A and H in Figure 1 and exits from sections C and G, while the cathodic gas enters from sections B and E and exits from sections D and F. Figure 14 shows the temperature distribution (design 4) compared with that in the initial design. The temperature profile becomes symmetric. The minimum temperature becomes close to the cathode inlet temperature, 851 K, which is due to the much large mass flow rate at the cathode with respect to the mass flow rate at the anode. The maximum temperature at $R=24$ mm shifts from the cell number 8 to the cell number 8, i.e. the center of the stack, and drops to about 882 K. This means that the temperature difference in the axial direction becomes close to 30°C .

Figure 15 shows the temperature profile in the cell number 8. Here the largest temperature gradients in transversal directions occur. The difference between maximum and minimum temperature in the cell is similar to that in case 1: 32°C instead of 33°C .

The average power density increases to about 340 W/m^2 , which means about 18% larger than the initial design. This value can be further increased by increasing the inlet temperature of both the anodic and cathodic gases. In the design 5, an increase of 10°C has been considered. It is shown in figure 13 that the axial temperature profile shifts above almost uniformly. The corresponding value of the average power density increases to 344 W/m^2 , and can be further increased as the maximum temperature is below the value obtained for the design 1.

The power density distribution is shown in figure 16. With respect to the design 1, there is a significant reduction in the maximum power density, from 612 W/m^2 to 485 W/m^2 and an increase in the minimum power density, from 136 W/m^2 to 216 W/m^2 . There is a more homogeneous distribution at stack level and a cell level: in design 1, the difference in power density occurring in the inner and outer parts of cell 10 is about 380 W/m^2 , while in design 5, this is reduced in cell 8 to about 240 W/m^2 . Concerning the stack, in design 1 there is a large difference in the average power density produced by the various cells: about 315 W/m^2 in the cell number 10 and about 230 W/m^2 in the cell number 1. In design 5, this difference is reduced of 55%: about 357 W/m^2 in the cell number 8 and about 310 W/m^2 in the cell number 1.

The temperature gradients in the cell number 8, are similar to that shown for the design 4. Small additional reductions may be achieved by acting on the cathodic mass flow rate to the different cells, as shown for the design 3.

Table 4 summarizes the main results obtained with the proposed changes in the stack design. Changes in the cathodic gas distribution produces positive effects on the temperature gradients (compare design 2 and 1) but reduction in the stack efficiency. This is because the average temperatures in the cells reduce. In order to increase the efficiency it is possible to increase the inlet temperature of reactants (compare design 3 and design 2). This has additional positive effects on the temperature gradients. Additional improvements in the efficiency can be achieved by adopting a fluid distribution that generates a symmetrical axial temperature profile, which is obtained through double side fluid supply. This design dramatically increases efficiency and reduces axial gradients (compare designs 4 and 5 to the other designs). Radial gradients slightly increase with respect to designs 2 and 3, but this can be improved by increasing the cathodic gas flowing to the central cells with respect to that flowing to the boundary cells. Fuel utilization does not change significantly in the various designs.

CONCLUSIONS

In this paper, a 3D model of a molten carbonate fuel cell stack composed of 15 circular cells is presented. The simulations highlight some issues related with cell and stack operation. At stack level, issues are mainly related with large temperature gradients which

causes differences in the performance of the various cells and may affect their lifetime. Fluid distribution is shown to be crucial in order to improve the design. Two different strategies, that can be applied together, are analyzed. The first one consists in increasing the cathodic flow at the cells with larger temperature. The main advantage consists in the reduction of the temperature gradients. With the examined designs, axial gradients are reduced of about 21% with respect to the initial design, while transversal gradients of about 36%. The second strategy consists in supplying the anodic and cathodic gases from two sides of the stack. The main advantage is a large increase in the average power density, about 18% with respect to the initial design. In addition, the axial temperature gradient is reduced of about 72%. As no major effect on the transversal gradients is observed, the combination of the two strategies may be recommended.

ACKNOWLEDGEMENTS

This work has been funded by ENEA within the framework of a collaboration between ENEA, FN and Politecnico di Torino. The authors would like to acknowledge the personnel of “Fabbricazioni Nucleari S.p.A” for their help and useful discussion.

REFERENCES

- [1] B. Bosio, P. Costamagna, F. Parodi. Modeling and experimentation of molten carbonate fuel cell reactors in a scale-up process. *Chemical Engineering Science* 54 (1999) 2907-2916
- [2] E. Arato, B. Bosio, R. Massa, F. Parodi. Optimisation of the cell shape for industrial MCFC stacks. *Journal of Power Sources* 86. 2000:302–308
- [3] F. Yoshida, T. Abe, T. Watanabe. Numerical analysis of molten carbonate fuel cell stack performance: diagnosis of internal conditions using cell voltage profiles. *Journal of Power Sources* 87. 2000: 21–27
- [4] M. Gundermann, P. Heidebrecht, K. Sundmacher. Physically Motivated Reduction of a 2D Dynamic Model for Molten Carbonate Fuel Cell (MCFC). *Fuel Cells* 08, 2008, 2: 96-110.
- [5] M. Fermeglia, A. Cudicio, G. De Simon, G. Longo, S. Priol. Process Simulation for Molten Carbonate Fuel Cells. *Fuel Cells* 2005, 5, 1: 66-79.
- [6] J.H. Koh, B.S. Kang, H.C. Lim. Analysis of Temperature and Pressure Fields in Molten Carbonate Fuel Cell Stacks. *AIChE Journal*, 2001. 47, 9: 1941-1956.
- [7] P. Heidebrecht, K. Sundmacher. Molten carbonate fuel cell (MCFC) with internal reforming: model-based analysis of cell dynamics. *Chemical Engineering Science* 58 (2003) 1029 – 1036
- [8] J.H. Koh, H.K. Seo, Y.S. Yoo, H.C. Lim. Consideration of numerical simulation parameters and heat transfer models for a molten carbonate fuel cell stack. *Chemical Engineering Journal* 87 (2002) 367–379
- [9] W. He, Q. Chen. Three-dimensional simulation of a molten carbonate fuel cell stack under transient conditions *Journal of Power Sources* 73. 1998:182–192
- [10] M. Mangold, M. Sheng. Nonlinear Model Reduction of a Two-Dimensional MCFC Model with Internal Reforming. *Fuel Cells* 2004. 4: 68-77
- [11] C. Massano, A. Sciacovelli, V. Verda (2009). Detailed Model of Molten Carbonate Fuel Cell Stacks. 22nd International Conference on Efficiency, Cost, Optimization Simulation and Environmental Impact of Energy Systems. August 31 – September 3, 2009, Foz do Iguaçu, Paraná, Brazil
- [12] M. Pfafferodt, P. Heidebrecht, K. Sundmacher. Stack Modelling of a Molten Carbonate Fuel Cell (MCFC). *Fuel Cells* 2010: 1-17
- [13] Brouwer J., Jabbari F., Leal E.M., Orr T. (2006). Analysis of a molten carbonate fuel cell: Numerical modeling and experimental validation. *Journal of Power Sources* 158: 213–224
- [14] C. Amelio, G. Diaz, E. Ferrari, E. Ghisolfi, L. Mannarino, C. Spadaro, E. Poskovic, S. Baccaro (2009). A New Approach to MCFC Ceramic Matrixes Manufacturing and Laboratory Small scale Stack Testing, Development of Innovative SOFC Cell Porous Components. European Fuel Cell Conference. Paper EFC09-17166.
- [15] L.Yu, G. Ren, X. Jiang. Experimental and analytical investigation of molten carbonate fuel cell stack. *Energy Conversion and Management* 49 (2008) 873–879
- [16] D. Marra, B. Bosio, E. Arato. Fluid-dynamic characterisation of MCFC gas distributors. *Chemical Engineering and Processing* 48 (2009) 797–807
- [17] A. Sciacovelli, V. Verda (2010) Entropy Generation Minimization for the Optimal Design of the Fluid Distribution System in a Circular MCFC. *Proceedings of ECOS 2010*. Lausanne, Switzerland.
- [18] T.i Okada, S. Matsumoto, M. Matsumura, M. Miyazaki, M. Umeda (2006). Gas distribution in molten-carbonate fuel cells. *Journal of Power Sources* 162: 1029–1035
- [19] L. Zhou, H. Lin, B. Yi, H. Zhang (2007). Study on a new structure of the separator plate assembly for molten carbonate fuel cell (MCFC) stacks. *Chemical Engineering Journal* 125: 187–192
- [20] P. Yuan (2008). Effect of inlet flow maldistribution in the stacking direction on the performance of a solid oxide fuel cell stack. *Journal of Power Sources* 185: 381–391.

- [21] Krishna R., Wesseling J. A. (1997). The Maxwell-Stefan approach to mass transfer. Chemical Engineering Science, Vol. 52, No. 6, pp. 861-911.
- [22] R.B. Bird, W.E. Steward, E.N. Lightfoot, Transport Phenomena, J. Wiley & Sons, New York, 1960
- [23] S.H. Chan, K.A. Khor, Z.T. Xia, A complete polarization model of a solid oxide fuel cell and its sensitivity to the change of cell components thickness, J. Power Sources 2001; 93: 130–140.
- [24] Fuller E.N., Schettler P.D., Giddings J.C. (1966). A new method for prediction of binary gas-phase diffusion coefficients. Industrial and Engineering Chemistry, Vol. 58, No. 5, pp. 18-27.
- [25] Z. Li, H. Devianto, H. Kwon, S. P. Yoon, T. Lim, H. Lee (2010). The catalytic performance of Ni/MgSiO₃ catalyst for methane steam reforming in operation of direct internal reforming MCFC. Journal of Industrial and Engineering Chemistry 16: 485–489.
- [26] J. Jewulski and L. Suski (1984) Model of the isotropic anode in the molten carbonate fuel cell. Journal of Applied Electrochemistry, 14: 135-143.
- [27] R.C. Reid, J.M. Prausnitz, B.E. Poling (1987) The properties of gases and liquids, 4th ed. McGraw-Hill, Inc. New York.
- [28] Sciacovelli A., Verda V. (2009) Entropy generation analysis in a monolithic-type solid oxide fuel cell (SOFC). Energy 34. 850-865.
- [29] J.O.M. Bockris, A.K.N. Reddy, Modern Electrochemistry, vol. 2, Plenum Publishing Corporation, New York, NY, 1973, pp. 845–1136.
- [30] G. Wilemski (1983). Simple Porous Electrode Models for Molten Carbonate Fuel Cells. Journal of Electrochemical Society, 130, 117-121.
- [31] A. Wijayasinghe, C. Lagergren and G. Bergman (2002) New Cathode Materials for Molten Carbonate Fuel Cells. Fuel Cells 3-4, 181-187.
- [32] M. Yoshikawa, A. Bodén, M. Sparr, G. Lindbergh (2006) Experimental determination of effective surface area and conductivities in the porous anode of molten carbonate fuel cell. Journal of Power Sources 158: 94-102
- [33] Sciacovelli A., Verda V. (2010) Entropy Generation Minimization for the Optimal Design of the Fluid Distribution System in a Circular MCFC. Proceedings of ECOS 2010, June 14- 17, 2010, Lausanne, Switzerland. pp. 1-8.
- [34] Bejan, A.; Lorente, S. (2007). Constructal tree-shaped flow structures. Applied Thermal Engineering. 27, 4: 755-761

List of Tables

Table 1. Stack dimensions

Table 2. Model parameters

Table 3. Characteristics of the anodic and cathodic gases feeding the stack

List of figures

Figure 1. Mesh of the computational domain

Figure 2. Schematic of a single fuel cell

Figure 3. Cross sections A-A and K-K of the fuel cell.

Figure 4. Temperature profiles in the cell for grid independence test.

Figure 5. Polarization curve of single cell

Figure 6. Power density distribution in the stack [W/m²]

Figure 7. Hydrogen mass fraction distribution

Figure 8. Oxygen mass fraction distribution

Figure 9. Axial temperature profile in the stack (K)

Figure 10. Temperature distribution (in K) in the cell number 10

Figure 11. Effect of temperature on the power density for three different reactant concentrations

Figure 12. Axial temperature profile in the stack for designs 1-3.

Figure 13. Temperature distribution in cell number 10 for the design 3.

Figure 14. Axial temperature profile in the stack for designs 1, 4 and 5

Figure 15. Temperature distribution in cell number 8 for the design 4.

Figure 16. Power density distribution in the stack corresponding with design 5 [W/m²]

Height	101.25 mm
External radius	95 mm
Anodic inlet duct diameter	6 mm
Cathodic inlet duct diameter	6 mm
Radial ducts length	22.5 mm
Radial ducts cross section	5 mm ²
Anode thickness	0.5 mm
Cathode thickness	0.5 mm

Table 1. Stack dimensions

Thermal conductivity	Anode	$78 \text{ W m}^{-1} \text{ K}^{-1}$
	Cathode	$0.9 \text{ W m}^{-1} \text{ K}^{-1}$
Porosity	Anode	50% [15]
	Cathode	55% [15]
	Electrolyte	$2 \text{ W m}^{-1} \text{ K}^{-1}$ [30]
Pre exponential factor σ_0	Electrolyte	$3637 \Omega^{-1} \text{ m}^{-1}$ [30]
Apparent activation energy E_k for eq. (12r)	Electrolyte	3016 K^{-1} [30]
Electrical conductivity	Cathode	28 S m^{-1} [31]
Electrical conductivity	Anode	48 S m^{-1} [32]
Permeability	Anode	$3.2 \times 10^{-12} \text{ m}^2$
	Cathode	$1.2 \times 10^{-10} \text{ m}^2$

Table 2. Model parameters

	Anodic gas	Cathodic gas
Temperature	753 K	863 K
Mass Flow rate	$1.82 \cdot 10^{-4}$ kg/s	$2.22 \cdot 10^{-3}$
Mass fractions	H ₂ 9.6%	O ₂ 14.1%
	H ₂ O 40.5%	N ₂ 63.7%
	CO 44.7%	CO ₂ 23.2%
	CH ₄ 5.2%	

Table 3. Characteristics of the anodic and cathodic gases feeding the stack

Design	Efficiency	Axial temperature difference (°C)	Radial temperature difference (°C)
Design 1 (standard)	39.56%	105	33
Design 2 (reduced diameters of radial ducts)	37.34%	95	21
Design 3 (Design 2 + DT = 10°C at anodic inlet)	38.60%	86	21
Design 4 (symmetric)	46.85%	30	32
Design 5 (symmetric + DT = 10°C at anodic and cathodic inlet)	47.40%	30	32

Table 4. Effect of the various design improvements on the stack performance

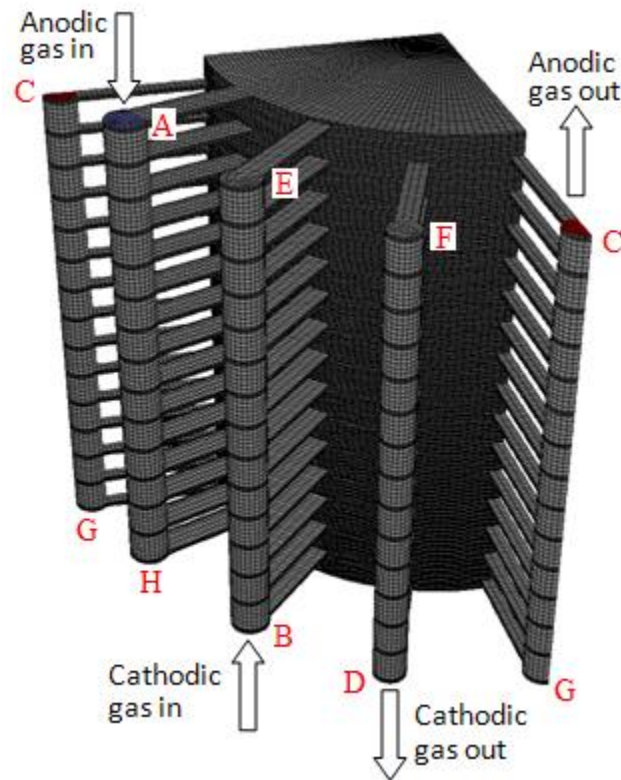


Figure 1. Mesh of the computational domain

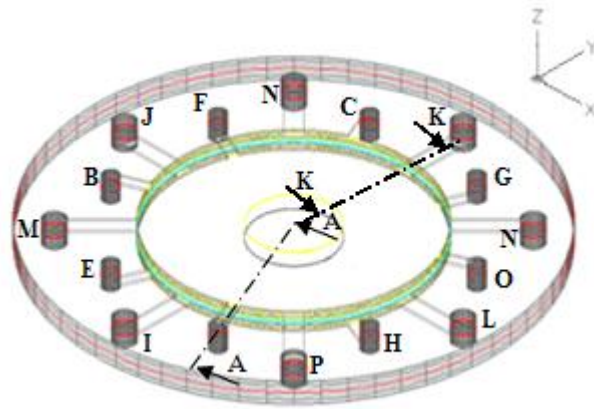


Figure 2. Schematic of a single fuel cell

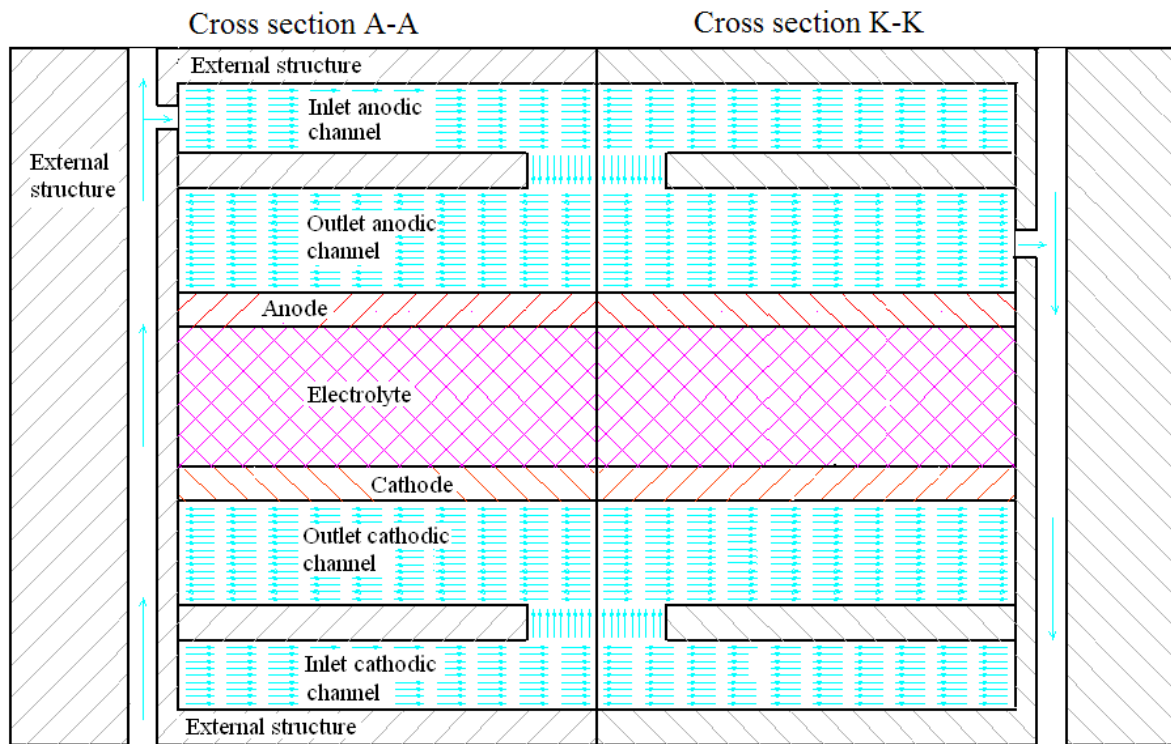


Figure 3. Cross sections A-A and K-K of the fuel cell.

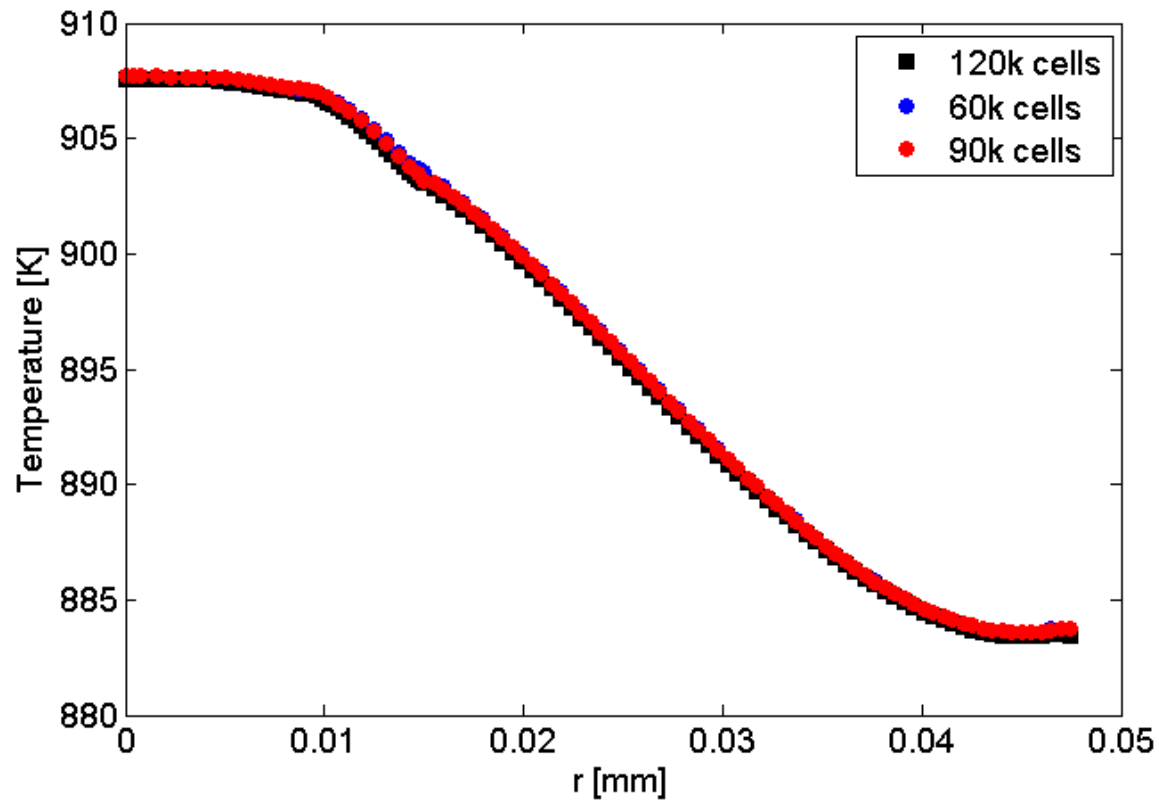


Figure 4. Temperature profiles in the cell for grid independence test.

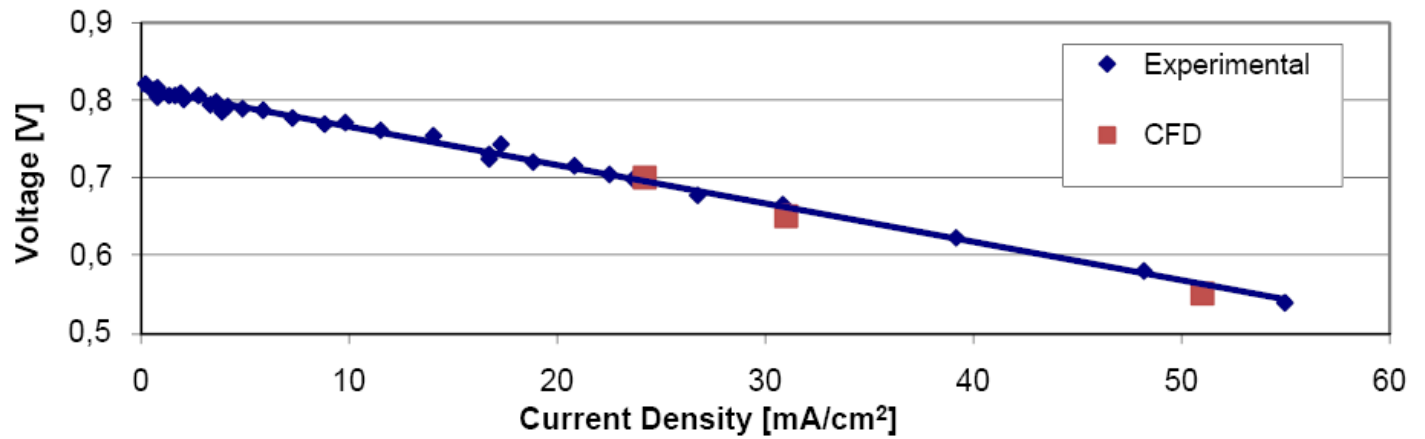


Figure 5. Polarization curve of single cell

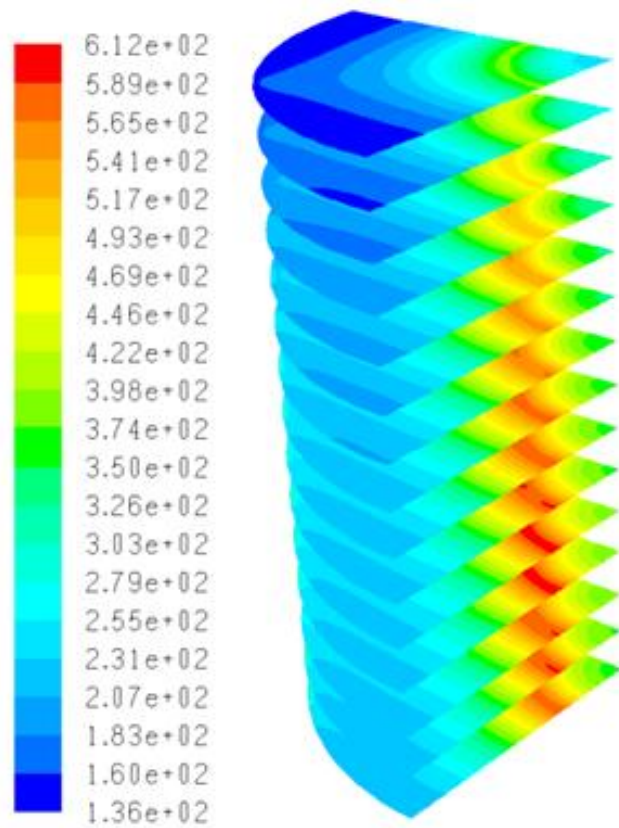


Figure 6. Power density distribution in the stack [W/m^2]

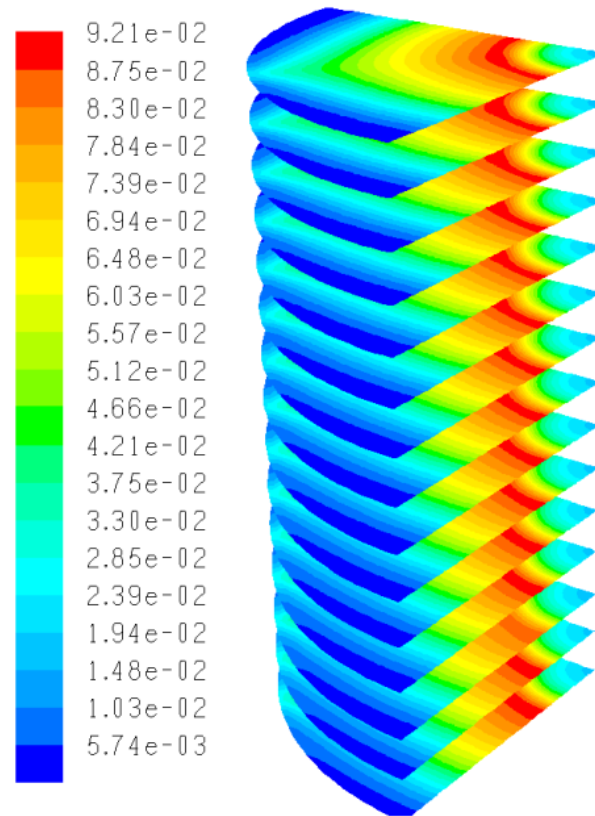


Figure 7. Hydrogen mass fraction distribution

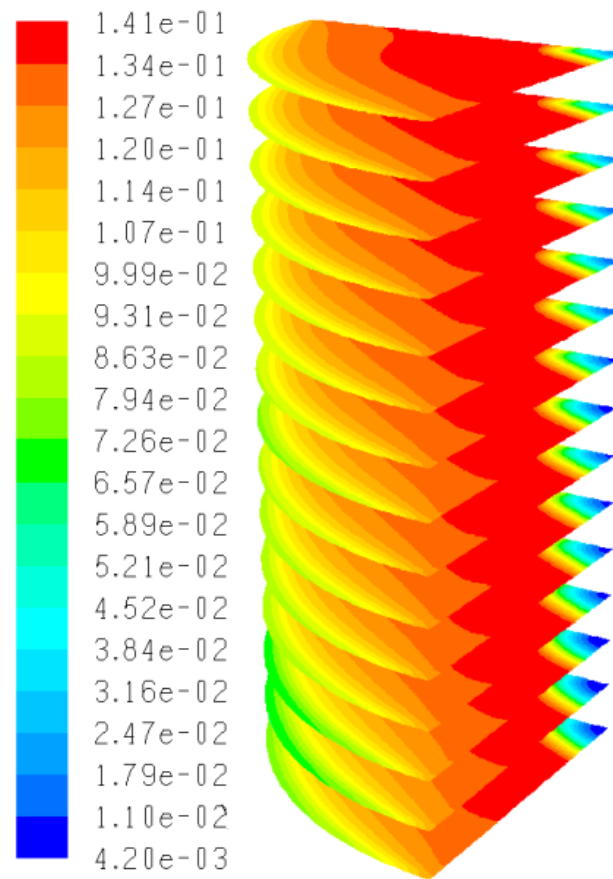


Figure 8. Oxygen mass fraction distribution

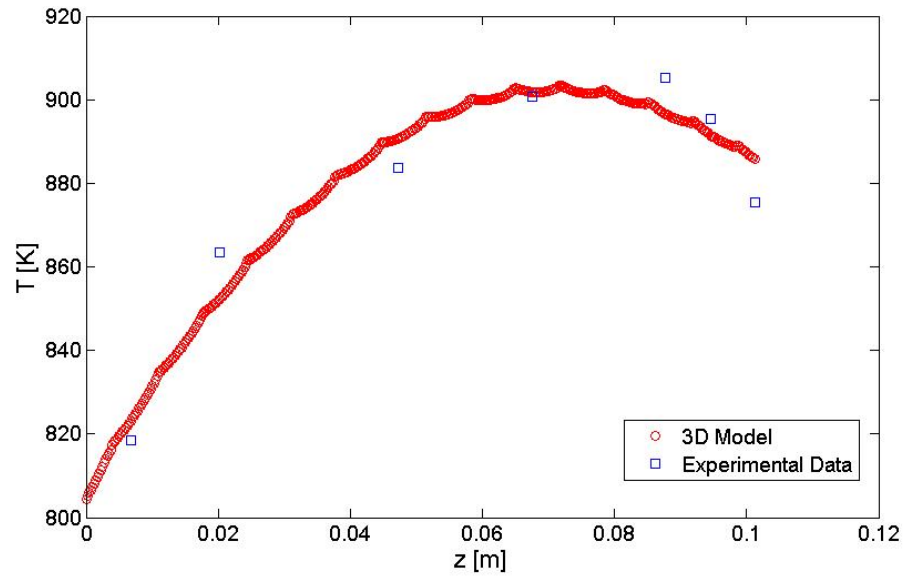


Figure 9. Axial temperature profile in the stack (K)

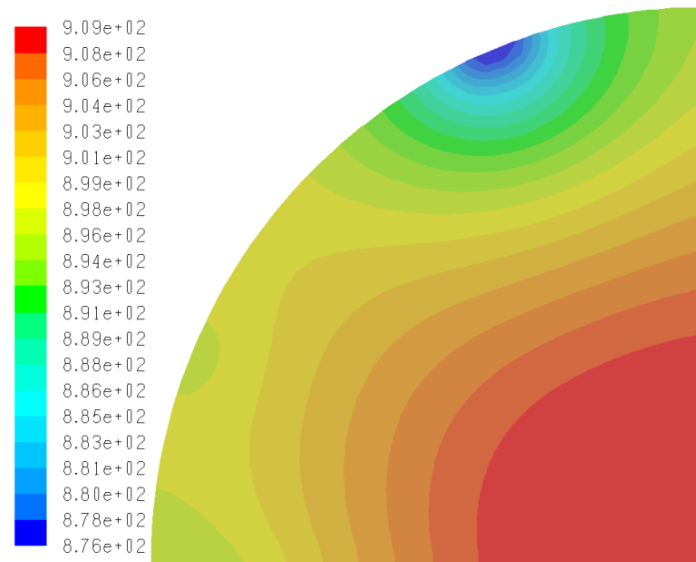


Figure 10. Temperature distribution (in K) in the cell number 10

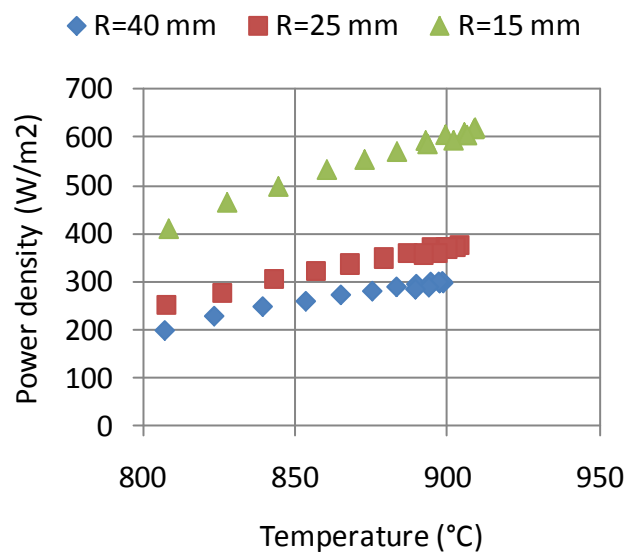


Figure 11. Effect of temperature on the power density for three different reactant concentrations

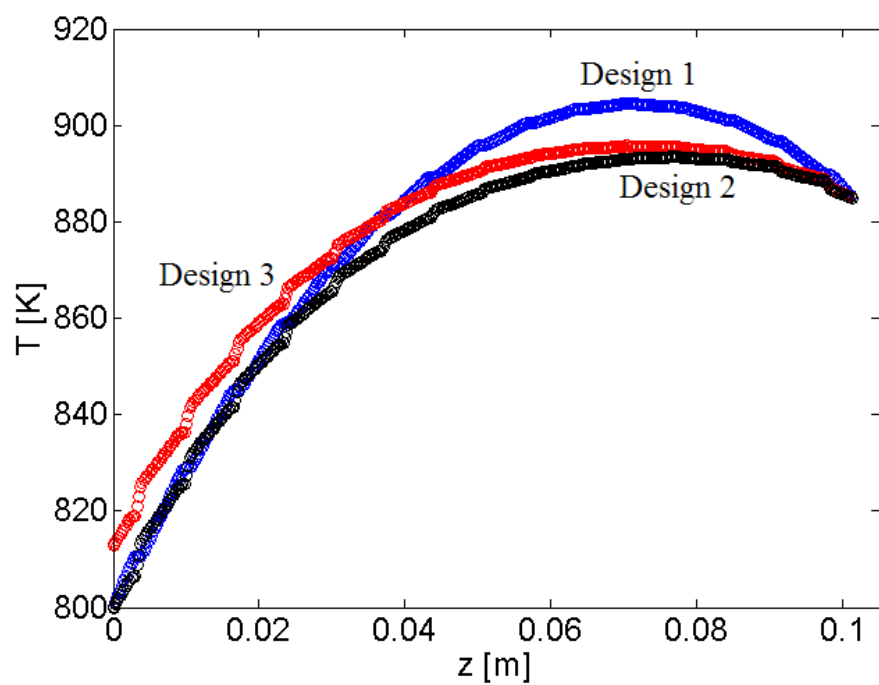


Figure 12. Axial temperature profile in the stack for designs 1-3.

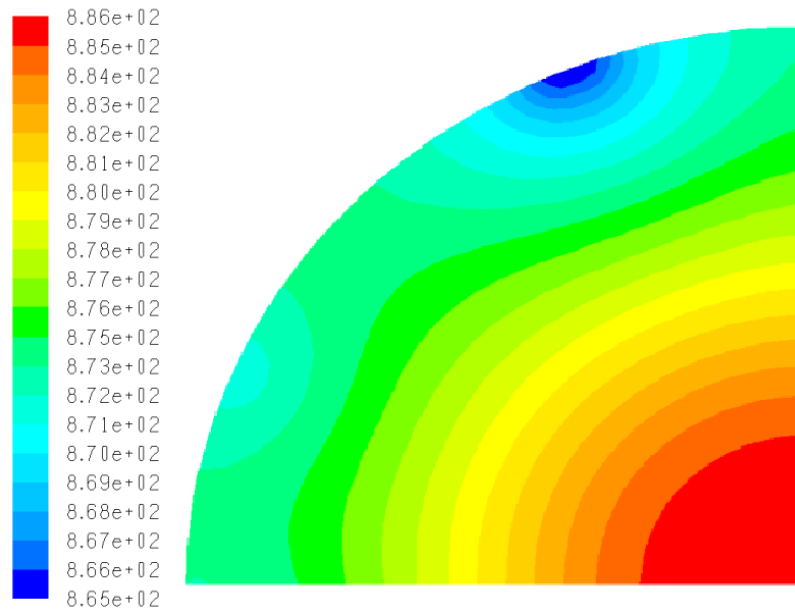


Figure 13. Temperature distribution in cell number 10 for the design 3.

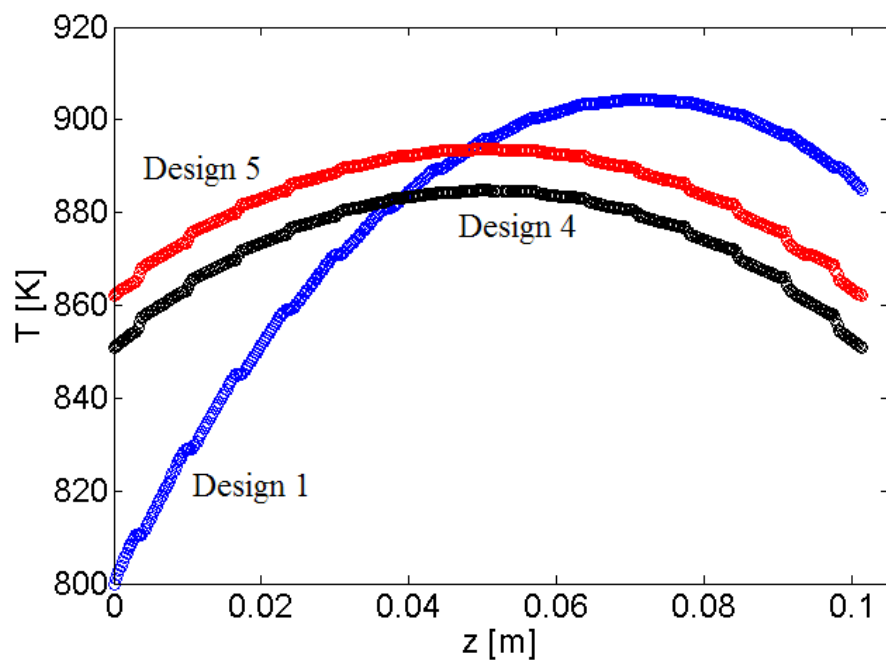


Figure 14. Axial temperature profile in the stack for designs 1, 4 and 5

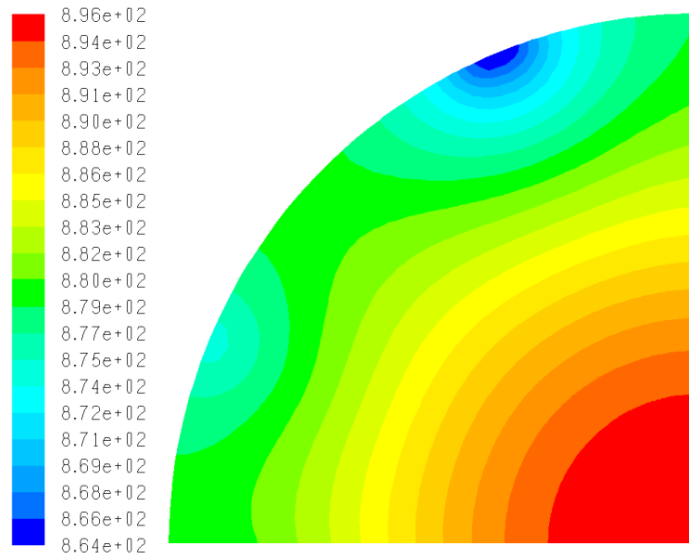


Figure 15. Temperature distribution in cell number 8 for the design 4.

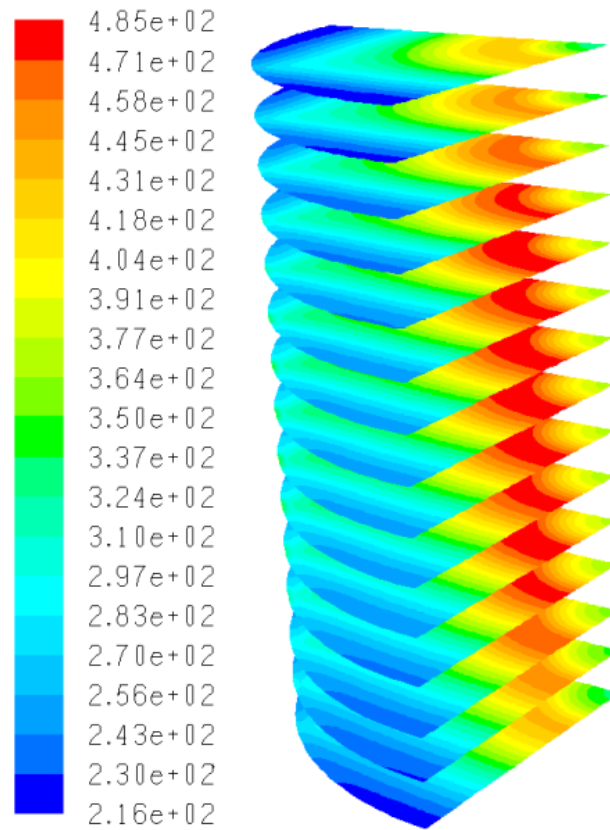


Figure 16. Power density distribution in the stack corresponding with design 5 [W/m^2]